Tuning the wettability of wire mesh column: pore-scale flow analysis

Mohamed Abdelraouf , Allan Rennie , Neil Burns , Louise Geekie , Vesna Najdanovic-Visak , Farid Aiouache

PII: S2666-8211(21)00096-X
DOI: https://doi.org/10.1016/j.ceja.2021.100181
Reference: CEJA 100181

To appear in: *Chemical Engineering Journal Advances*

Received date: 11 June 2021
Revised date: 16 August 2021
Accepted date: 5 September 2021

Please cite this article as: Mohamed Abdelraouf , Allan Rennie , Neil Burns , Louise Geekie , Vesna Najdanovic-Visak , Farid Aiouache , Tuning the wettability of wire mesh column: pore-scale flow analysis, *Chemical Engineering Journal Advances* (2021), doi: https://doi.org/10.1016/j.ceja.2021.100181

Tuning the wettability of wire mesh column: pore-scale flow analysis

Mohamed Abdelraouf[1], Allan Rennie[1], Neil Burns[2], Louise Geekie[2], Vesna Najdanovic-Visak[3,*], Farid Aiouache[1,*]

[1]Engineering Department, Faculty of Science and Technology, Lancaster University, Lancaster LA1 4YW, United Kingdom.

[2]Croft Filters Ltd, Taylor Business Park, Risley, Warrington WA3 6BL, United Kingdom.

[3]Chemical Engineering and Applied Chemistry, Energy and Bioproducts Research Institute, Aston University, Birmingham B4 7ET, United Kingdom.

[*]Corresponding authors: f.aiouache@lancaster.ac.uk, v.najdanovic@aston.ac.uk

Highlights

- Pore flow over mesh ring was successfully reproduced experimentally and by 3D modelling
- Droplet flow penetration and adherence to hydrophilic mesh opening were validated
- Droplet slip and accumulation as drips over hydrophobic mesh were validated
- Pore-scale profiles of wetting efficiency and liquid holdup reproduced the macroscale profiles
- Pore scale model agreed with macro-scale models of the liquid holdup and effective area

Abstract

The pore-scale behaviour of liquid flow over wire mesh stainless-steel packing of variable contact angle is relevant for mass and heat exchanges in multiphase chemical systems. This behaviour was investigated by imaging experiments and 3D volume-of-fluid modelling. The surface of the wire mesh ring was modified by alumina coating to reach both hydrophilic and hydrophobic characteristics. The cycle of capillary droplet flow over the uncoated ring exhibited penetration of the hydrophilic mesh openings, adherence to the surface of the ring and accumulation as drips at the bottom region of the rings. However, over the hydrophobic ring, the droplet exhibited low adherence to the ring surface, accumulation at the top surface of the ring, no penetration of the openings, slip by the gravitational forces over the vertical curvature and accumulation as drips at the bottom region. In agreement with the classical observations at the macroscale, the observations at the pore-scale confirmed the increase of the wetting efficiency, liquid holdup and effective surface area at increased liquid flowrate and reduced contact angle. The 3D model was in reasonable agreement with Stichlmair's model for the liquid holdup, particularly in the hydrophilic zone of the contact angle and low flow as well as in a reasonable agreement with Linek's model for effective area, particularly in the hydrophobic range of the contact angle.

Keywords

Novel column packing, wettability, contact angle, liquid dispersion, process intensification, Dixon

Nomenclature

a_e	Effective area (m^2/m^3)
a_p	Packing area per unit volume (m^2/m^3)
c	Capillary width (m)
d_p	Packing diameter (m)
G	Chemical potential density (J/m^3)
g	Gravity constant (m/s^2)
h_L	Liquid holdup (-)
F_g	Gravitational forces (N)
F_{r_L}	Froude number (-)
F_s	Surface tension forces (N)
p	Pressure (Pa)

T	Viscous deformation tensor
u_0	Liquid inlet velocity (m/s)

Greek letters

ρ_L	Liquid Density (kg/m^3)
μ_L	Liquid viscosity (kg/m.hr)
σ_L	Surface tension coefficient (N/m)
β	Slip length (m)
ϕ	Phase field variable (-)
λ	Mixing energy density (N)
γ	Mobility parameter (-)

1. Introduction

Packed bed columns are largely employed in multiphase systems as they are estimated to account for 40-70 % of the capital and operating costs of modern process industries. The improvement of liquid flow inside the packed columns, in terms of relevant flow characteristics such as dispersion of the liquid phase and wetting efficiency of the packing, has been extensively investigated owing to the impacts of these characteristics on process design from both economic and environmental perspectives. An example of such packing is Dixon rings which are made of a wire mesh grid of cylindrical shape that is extended to a flat grid along the longitudinal direction of the ring. As shown in Fig. 1, the mesh structure of the Dixon ring offers extra paths for gas to flow into the ring through the openings of the grids, resulting in the high effective surface area, that is of utmost importance in the catalytic and gas-liquid separation applications [1] [2].

Fig. 1: Stainless steel packing – Dixon ring ¼" diameter

The wetting efficiency of the packing is a critical design parameter as it affects the gas-liquid interface where the chemical process takes place as well as the patterns of flow of multiphase systems. It shapes variations of the liquid flow under various regimes (i.e. droplets, rivulets, channelled or trickle types), directly influencing mass and heat transfer phenomena [3]. The wetting efficiency is defined by the contact angle, which is the angle between the tangent to the interface of a droplet and the solid walls. When the contact angle is higher than 90°, a hydrophobic non-wetted surface is obtained, whilst a hydrophilic wetted surface is reached when it is less than 90°. The wetting efficiency is entangled by the hysteresis of the liquid distribution over a surface, the operating flow and the type of packing (i.e. materials and geometries). Early efforts were made by Billet and Schultes [4] on modelling the wetting efficiency of a randomly distributed packing using a large experimental database to derive correlations on the liquid holdup, effective surface area and mass transfer coefficient. An improved model was later developed by Rocha *et al*. [5] for multichannel flow through structured packing. The relevance of properties such as the contact angle (θ) and the size of the corrugations was reported and a model of the flow at microscale was highlighted based on correlations of the liquid holdup, the partial wetting and the liquid film thickness. Lambert & Gonzalez [6] used a bouncing droplet over a super-hydrophobic surface to demonstrate that the characteristics of a solid surface affect the shape and the pattern of flow. Dong *et al*. [7] developed an effective strategy to control the overflow of liquid on a micro-nano structured super-hydrophilic surface. Haroun *et al*. [8] and Ataki & Bart [9] investigated the wetting efficiency of structured packing, namely Mellapak 250.X and Rombopak-4M, respectively. The flow characteristics were reported by 3D simulation that captured the variations of motion of the gas-liquid interface. They combined the volume of fluid (VOF) model and the Eulerian-Eulerian

model to investigate the effects of operating flow and properties of the liquid on the behaviour of flow variations, and reported modifications of existing correlations on the liquid holdup and the effective surface area for the structured packing. They emphasised the relevance of the θ on the flow regime. The higher the θ is, the more responsible it is for changing the flow from a trickle to bubble flow. Other works showed the feasibility of this modelling approach. The surface wetting ratio of a single catalyst particle was studied by Du *et al*. [10] and Augier *et al*. [11]. The former studied the effect of different operating flow rates, liquid viscosities and contact angle on the liquid film thickness and the latter investigated the reactive efficiency of different catalyst shapes. Overall, few studies investigated the wetting efficiency of gas-liquid flow in packed columns using a combination of spatially resolved experimental imaging and 3D modelling. Such an approach would demonstrate the relevance of conducting evaluations at the microscale level and help to understand the changes in flow-packing interactions.

One method that can be used to adjust the surface wettability is by applying a surface modification of the packing using a uniform coating of hydrophobic or hydrophilic nature, depending on the application of interest. Kumar *et al*. [12] compared the liquid hold up and the axial dispersion in packed beds of hydrophobic and hydrophilic types using the radiotracer technique and confirmed the anticipated high dispersion in the case of hydrophobic packing and the high holdup in the case of hydrophilic packing. Yan & Gao [13] investigated the effect of the hysteresis of the contact angles on the interfacial wettability for a packing that was coated by the spray and dipping methods. It proved that the lower the contact angle is, the less pressure drop occurs, resulting in high weeping rates. The hydrodynamics and mass transfer performances in a rotating packed column with a hydrophobic mesh were investigated by Zhang *et al*. [14] using a high-speed camera. They evaluated the dispersion by observations of the cone angle that was generated from the splashes of droplets-solid packing interactions. The results showed that a hydrophobic mesh was more capable of spreading the liquid and thus improving the mixing capabilities. Ma *et al*. [15] studied the wetting efficiency in a rotating packed bed of Al_2O_3 coated stainless steel mesh. In comparison to the uncoated stainless-steel mesh, the coated wire showed a higher wetting ratio, leading to an increase in the efficiency of mass transfer by 45.7 %. Su *et al*. [16] used a series of stainless-steel substrates to study the wettability in a rotating bed reactor. The wetting efficiency was related to the surface hardness and surface free energy which allowed an understanding of the role of the coating material on the wettability behaviour.

The opportunity to apply computational fluid dynamics (CFD) as a tool to model the flow distribution in packed columns has enabled significant progress in studying the wetting efficiency for fluid-solid interactions of various geometries and solid types. The VOF approach has principally

been used and was conducted in combination with the Eulerian-Eulerian model, allowing capture of the interphase of surfaces between the liquid and the solid packing [17]. The spatial resolution of these methods helped link the complex geometrical configuration of the packing and operational parameters to patterns of the flow and thus assess interactions of the gas, liquid and solid phases of multiphase systems [18] [19].

Since the wetting performance and liquid dispersion are critical information to anticipate, the development of surface characteristics of a packing that would be tuneable is essential for multiphase flow. The study at the microscale level of packing is a promising approach to understand the phenomena that take place and predict those that occur at large scales. In addition, the visualisation of the dynamics of the wetting at the macroscale level is still not sufficiently mature since existing methods that allow observations of time-integrated data while the dynamics of the flow occurs, particularly at low velocities, where the time resolution of observation is critical, are not straightforward [20] [21].

In this work, spatially resolved procedures based on imaging using a Charged Couple Device (CCD) camera and 3D modelling, that combines the VOF and Eulerian-Eulerian models, are used to investigate the wetting behaviour of the Dixon ring subject to the multiphase flow under a trickle flow regime. The trickle flow exhibits partial wetting due to preferential channelling, leading to mal-distribution and uneven mixing. The local flows around an element of coated and uncoated Dixon rings are visualised by experimental imaging and compared with those obtained by 3D CFD simulation. The wetting efficiency of the Dixon rings and the liquid holdup, which have an impact on the solid-liquid interfacial area and the dispersion of the liquid, are investigated through a parametric study by varying the liquid flow rate and the contact angle relevant to hydrophobic and hydrophilic types of packing surfaces.

2. 3D CFD model and discretisation

2.1. Governing equations

The flow of the gas and liquid phases in the packed column was simulated by coupling the Navier-Stokes model of fluid flow with the VOF method and solving by the Finite element method. The Laminar Two-Phase Field module, COMSOL Multiphysics 5.3a, was used to execute these simulations using a computer server with 512 GB RAM. The fundamentals of the phase-field model are described as follows and more details about the model can be found elsewhere [22].

The VOF captured the diffuse interface between the two immiscible fluids (i.e. water and air) and used the mixing and the storage energies at the interface by decomposition of the Cahn-Hilliard second-order partial differential equations. The model was set to be controlled by the phase-field variable (ϕ), considering the synergies of mixing and storing energies at the interfacial region, and ensuring minimisation of the total energy correctly [23].

The phase-field model was simplified by assuming incompressible Newtonian liquid, constant viscosity, isothermal environment and laminar flow (i.e. negligible turbulence effects due to low velocity). The continuity and momentum equations are expressed by Equations (1) and (2), respectively.

$$\nabla . u = 0 \quad (1)$$

$$\frac{\partial u}{\partial t}\ \rho + \rho(u.\nabla)u = [-pI + \mu(\nabla u + \nabla u^T) + F_g + F_s] \quad (2)$$

where p represents the pressure (Pa), ρ is the density (kg/m^3), u is the velocity vector (m/s), F_g and F_s are the gravitational and surface tension forces (N), respectively, and μ is the dynamic viscosity (kg/m.hr).

The phase-field model incorporates the effects of the volumetric forces, such as gravity and surface tension. The surface tension was represented by the mixing energy. The surface tension forces, which are distributed over the interface, were calculated using the phase-field variable (ϕ), as shown in Equations (4) and (5), respectively. Therefore, this computation avoided complex terms such as the surface curvature and the surface normal, which are typically required in other multiphase models (i.e. the level set model) [24].

$$F_g = \rho g \quad (3)$$

$$F_s = G\nabla\phi \quad (4)$$

$$G = -\nabla^2\varphi\lambda + \frac{\lambda(\varphi^3-\varphi)}{c^2} \quad (5)$$

where G is the chemical potential density (J/m^3), ϕ is the phase field variable (-), c ~~is,~~ is the capillary width (m) and λ is the mixing energy density (N).

Two additional equations were included in this model to capture the fluid interface. These equations calculate the phase field variable (ϕ) and phase-field help variable (ψ), as shown in Equations (6) and (7), respectively.

$$\frac{\partial\phi}{\partial t} + \nabla . u\phi = \nabla . \frac{\gamma\lambda}{c^2}\ \nabla\psi \quad (6)$$

$$\psi = -\nabla . c^2 \nabla\phi + (\phi^3 - \phi) + \frac{c^2}{\lambda}\frac{\partial f}{\partial \phi} \quad (7)$$

where $\frac{\partial f}{\partial \phi}$ is the phi-derivative of external free energy (-) and γ is the mobility parameter (m^3.s/kg).

The latter determined Cahn-Hilliard's diffusion time scale. It has to be selected carefully to maintain a constant interfacial thickness and to prevent overdamping the convective terms [25].

In the regions where fluids were segregated, i.e. no mixing, one fluid was set to take the element ϕ = 1 and the other fluid to take the element ϕ = -1. Conversely, the interface or the phase-field region was set in the range of these two boundary values, as expressed by using Equation (8).

$$-1 \leq \phi \leq 1 \quad (8)$$

The volume for each element should remain constant for incompressible fluids. Therefore, if one fluid would leave a tiny volume element due to the interfacial diffusion, the other fluid would occupy the same volume element and vice versa. This allows the phase-field model to consider the discrepancies in the physical properties, i.e. density and viscosity, in regions where gas and liquid are in contact. The local density and dynamic viscosity of the mixture were calculated from local volume fraction values inside each cell of the calculation domain and areas described by Equations (9) and (10):

$$\rho = \rho_1 V_{f_1} + \rho_2 (1 - V_{f_1}) \quad (9)$$

$$\mu = \mu_1 V_{f_1} + \mu_2 (1 - V_{f_1}) \quad (10)$$

The subscripts 1 and 2 in Equations (9) and (10) refer to water and air, which were considered as Fluid 1 and Fluid 2, respectively. The volume fraction (V_f) was computed by Equations (11) and (12):

$$V_{f_1} = \frac{\phi + 1}{2} \quad (11)$$

$$0 \leq V_{f_1} \leq 1 \quad (12)$$

2.2. Model setup

To solve the governing differential equations for gas and liquid phases, the initial values and the boundary conditions have to be defined for all the domains and the boundaries. The initial values were specified by assuming that only the gas phase was present in the column, whilst the liquid phase was precluded from entering the column (*i.e.* at t = 0: V_{f_2} = 1 and $V_{f_1} = 0$). The inlet boundary was defined through the inlet velocity (u_o) and the outlet boundary was defined through atmospheric outlet pressure. Details about the model characteristics are illustrated in Table 1.

Table 1: Parameters of the VOF model.

Multi-phase model	Volume of fluid
Fluid	Air-water
Contact angle	60°, 90°, 105° and 120°
Surface tension (N/m)	0.0729
Operating pressure (atm)	1
Operating temperature (K)	293
u_o (m/s)	0.15, 0.25, 0.35 and 0.5
Gas inlet velocity (m/s)	0.011
Thickness of the Dixon ring	0.003 m

A range of contact angles, from 60 to 120°, covering both hydrophobic and hydrophilic properties are illustrated in Table 1. These values were selected as they reflect interactions of typical solvents with modified or unmodified surface structures [26].

The boundary condition requires the calculation of the frictional forces ($F_{friction}$) using the slip length (β). As shown in Fig. 2, the interactions of the liquid with the solid surface were considered using the adhesive condition, which is known as the wetted wall boundary condition. This boundary condition allowed the definition of the constant static contact angle (θ). The wetted wall boundary condition was calculated by Equation 13. The geometry, as shown in Fig. 3 (a), included the column (i.e. height and diameter were set to 18 and 4.8 mm respectively) and the inlet nozzle (i.e. size of 1.5 mm). A Dixon ring element was cut to have a diameter of 3 mm and length of 2 mm, and was then placed at the centre of the column, as shown in Fig. 3(a). Frictional force $F_{friction}$ was calculated according to Eq. (13):

$$F_{friction} = -\frac{\mu}{\beta}u \qquad (13)$$

where β and μ are slip length (m) and viscosity (kg/m.hr), respectively.

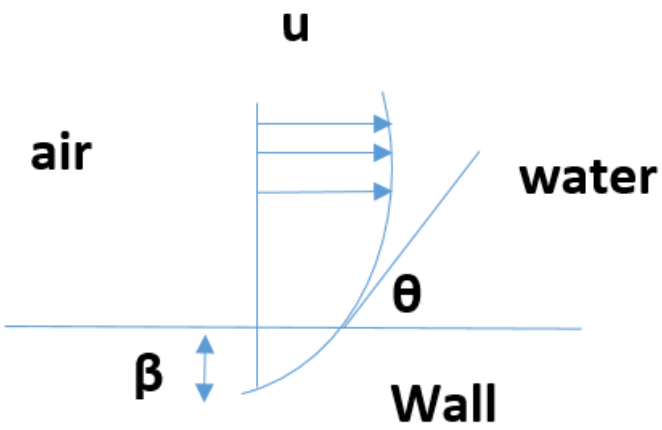

Fig. 2: Constant contact angle "θ" at the wall boundary condition.

A computer aided design (CAD) drawing of the Dixon ring geometry was provided by Croft Filters Ltd (Risley, UK). The CAD drawing required some modification in order to reduce the skewed elements occurring due to the intersections of the wires. The thickness of the cut of the Dixon ring was selected because it was found sufficient to observe the full flow of the drops through the openings or over the surface of the Dixon rings without overflow over the lateral sides. The intersections between the wires of Dixon rings had to be relaxed by 0.00001 m to avoid skewed meshing in both domain and boundary zones, as shown in Fig. 3(b).

.

a) b)

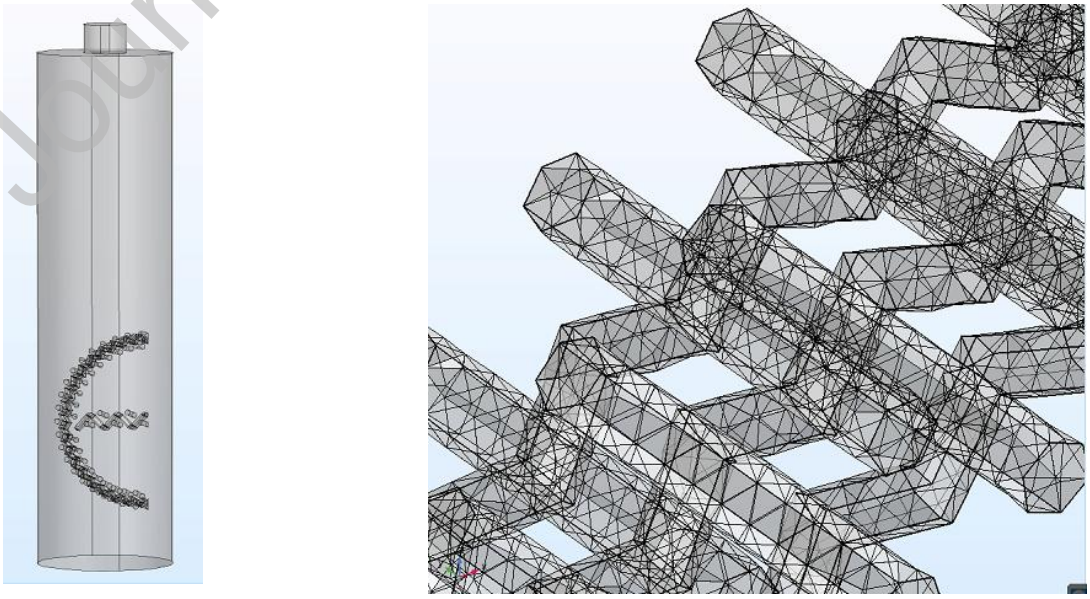

Fig. 3: a) Illustration of the geometry of the 3D model, b) GR2 mesh distribution at the intersection of the wires, pore to mesh size ratio is 3.

2.3. Solution procedure

The phase-field model included a phase initialisation step and a transient step. The phase initialisation study started the phase field variable (ϕ) and ensured that it was smoothly varying throughout the domain, while the transient step solved the momentum conservation and Cahn-Hilliard equations. Moreover, the time-dependent study iteratively solved several non-linear equations for every time step using Newton's approach. This approach evaluated the Jacobian function and its computationally expensive derivative. The default settings in COMSOL minimised the computational power by calculating the Jacobian derivative using a constant damping factor. However, this model was associated with a high degree of non-linearity due to the complex geometry of the Dixon rings, which generated skewed mesh elements. The initial simulations diverged when a constant damping factor was used in the calculation. It was then replaced by the dynamic damping factor, which was however computationally more expensive [27] [28].

The simulation started by discretising the fluid domain into many cells and the governing equations were then integrated for each cell. The differential equations were computed using an iterative solver (i.e. the generalised minimal residual solver) which was found to be effective and was then coupled with the geometric multigrid preconditioner to find numerical solutions for the non-symmetric matrices [29]. The preconditioner was used to coarsen the mesh using a multigrid, which reduced the order of the shape functions [30]. Other iterative solvers such as Flexible Generalized Minimal Residual method (FGMRES) and Biconjugate gradient stabilised method (BiCgStab) have been tested and provided similar results to the generalised minimal residual solver. The transient simulation was conducted using a time step of 0.005 s and convergence of relative tolerance of 0.01%. The simulation was conducted for a co-current gas-liquid flow configuration and the results of the flow pattern were described by the isosurface VOF value of 0.5.

3. Material and methods

3.1. Preparation and characterisation

In the previous work [31], a sol-gel alumina coating of uniform thickness of approximately 20 µm was applied to the Dixon rings. The same method was used to prepare the hydrophobic Dixon rings. Dixon rings ¼" made of stainless steel 316L were supplied by Croft Filters Ltd (Risley, UK) and were used as a substrate for the coating. The data on the structural size were provided by the supplier and are illustrated in Table 2.

Table 2: Uncoated and coated Dixon rings ¼" in structural data.

	Diameter (μm)	Mesh (standard)	Length (mm)	Aperture (μm)	Calcination temperature (K)	Dipping cycles
Uncoated wire mesh	165	60 × 60	30	258	-	-
Coated wire mesh	205	60 × 60	30	218	773	3

3.2. Experimental flow analysis over Dixon rings

The experiments were carried out to validate the VOF model and capture realistic data of the wetting efficiency for the coated and uncoated configuration. The uncoated Dixon rings were degreased in an ultrasonic bath at 100 W for 10 mins then dried at 373 K for 1 h. The coating was deposited by dipping Dixon rings in alumina sol-gel suspensions. Aluminium isopropoxide (AIP) was selected as a precursor and was hydrolysed with the ratio of 1:100 (mol AIP:mol H_2O) at 353 K. More details about the coating procedure are provided in previous work [31].

The experimental setup included a CCD camera (IMETRUM, video gauge) with 60 frames per second (fps) and resolution (640 x 480), flashlight, and image processing software (ImageJ). The experiments were operated at atmospheric pressure and ambient room temperature and were designed to reproduce the VOF model environment, as shown in Fig. 4. A syringe pump (Aladdin Programmable Syringe Pump, 1000-220) with a precision of 1.2×10^{-5} ml/min and a needle orifice of 2 mm were used to provide the desired flow, capillary droplets or liquid filaments. The liquid injection was held 12 mm apart from the Dixon ring and the injection speed was changed based on the desired flow. The experiments were repeated three times to enhance the qualitative comparison of the liquid flow direction over Dixon rings with the model results. Both distilled water and black dye were used, which helped discriminate the droplets from the rings using image processing Image J package. The Dixon rings were cleaned with acetone and dried before each experiment to remove any potential surface impurities. The time resolution of the camera was improved by capturing repetitive collisions of the droplets and capturing fine details of the collision and further dispersion of flow. A cycle of capillary droplet flow started when the droplet fell from the needle, impacted on the Dixon ring and then left it.

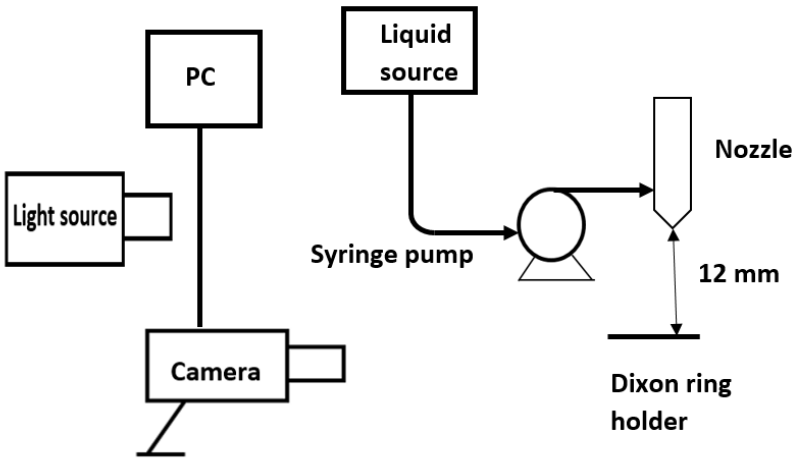

Fig. 4: A schematic representation of the experimental setup for flow imaging over Dixon rings: PC – personal computer, camera – (IMETRUM, video gauge), syringe pump (Aladdin Programmable Syringe Pump, 1000-220), liquid source – water 500 mL tank, nozzle (20 mm ID).

4. Results and discussion

4.1. Model validation

4.1.1. Flow over uncoated Dixon rings

The dynamics of the capillary droplets on an uncoated stainless steel Dixon ring at Weber number (W_e) of 0.23 at the nozzle and after collision with the Dixon ring wall are illustrated in Fig. 5 (a-d) and (e-h) by a series of snapshots from laboratory experiments and Dixon rings cut used in simulations. The dynamics of the impact of the droplet over the Dixon ring were driven by competition of the inertial forces and the surface tension forces, in particular, the flow velocity, surface tension and Dixon ring surface roughness. During the impact and spreading of the capillary droplet, the inertial forces were converted into viscous dissipation forces, allowing the creation of new surfaces of the liquid for further spreading over the Dixon ring.

The dropwise flow of water from the nozzle demonstrated the non-visco-elastic property of the flow and accumulated at the top part of the mesh openings for the uncoated rings. The droplets built up a liquid film and penetrated the grid by the formation of dripping drops inside the Dixon ring. The droplets were then obstructed by the horizontal grid at the centre of the ring at 0.2 s (Fig. 5 (b)) but continued filling the bottom region of the Dixon ring (Fig. 5 (c)). After 0.36 s, the bottom region became full and the liquid started to overflow through the sides at reduced velocity. This overflow led the droplets to reach the flooding conditions. The results from the model showed that the liquid was adhering to the ring until it reached the bottom section where the liquid was trapped and accumulated. The liquid film exhibited adherence to the uncoated ring, with no breakup and the thickness around the Dixon ring increased after each droplet until the liquid reached maximum

value after four impact cycles and then detached at 0.36 s, as shown in Fig. 5 (d). The CFD simulation (Fig.s 5 (e-h)) show dynamics of the impact of the droplets of a reasonable agreement with the experimental data. Both Figs. 5 (b) and (f) of 0.2 s time snapshots show the droplet trapped inside the ring. These figures were improved by adding boundaries around the droplets to discriminate the flow pattern (red line). The experimental droplet was however mainly located above the horizontal grid (b) while the ring simulation shows a uniformly distributed droplet inside the ring (Fig. 5 (f)). The two snapshots at 28 s and 36 s show the experimental droplet filling the bottom part of the ring and later accumulated underneath while the simulation droplets remained well adhered to the grid inside the ring. Overall, the flow patterns by the simulation appear to be built slightly faster, as they show the accumulated droplets being more developed.

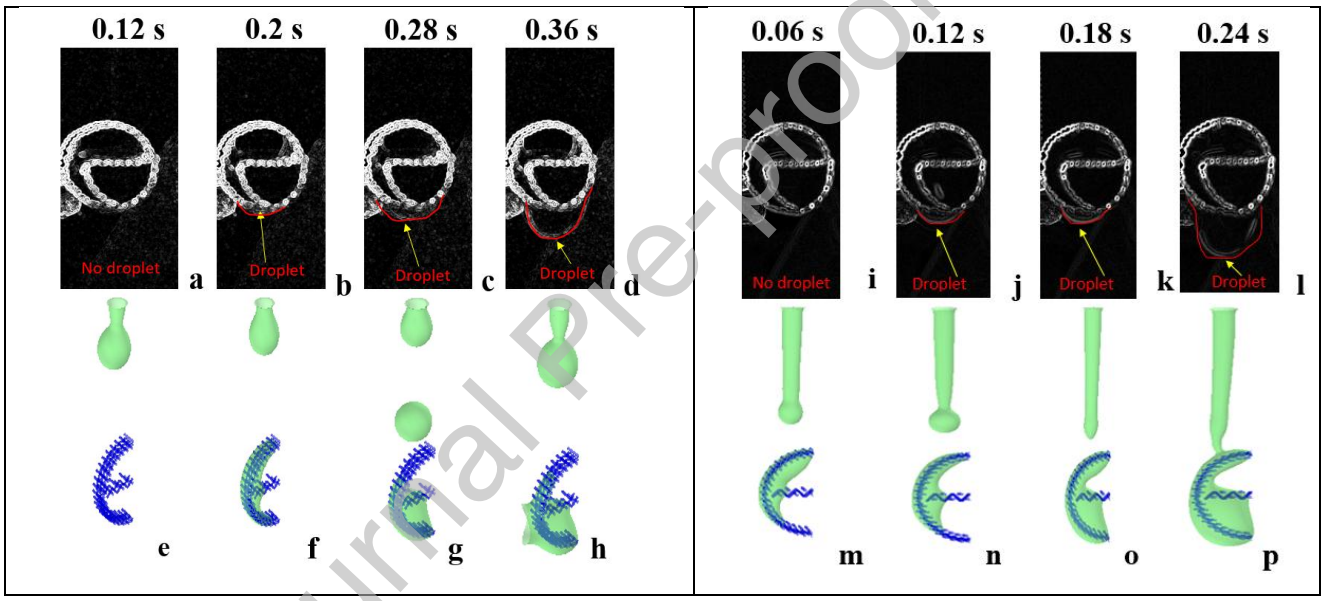

Fig. 5: Flow pattern comparison between the experimental and Snapshots of the impact of droplets (a-h) and filaments (i-p) on uncoated stainless steel Dixon ring for W_e= 0.23 : (a-d) experiments, (e-h) simulation (a & e) at 0.12 s, (b & f) at 0.2 s, (c & g) at 0.28 s and (d & h) at 0.36 s, and for W_e= 0.64 : (i-l) experiments, (m-p) simulation, , (i & m) at 0.06 s, (j & n) at 0.12 s, (k & o) at 0.18 s and (l & p) at 0.24 s.

When W_e was increased from 0.23 to 0.64, the same dynamics were observed as shown in Fig. 5 (i-l) (i.e. experimental droplet accumulation above the horizontal grid vs. uniform distribution through the ring of the simulation in Fig. 5 (m – p), accumulation of the experimental droplet at the bottom the ring vs. accumulation of simulation droplet inside the ring). Also, a continuous liquid stream occurred and fully developed at 0.24 s, as shown in Fig. 5 (l and p). The liquid flow pattern from the

experiments and the model reached a steady-state flow within a shorter time than that reached at W_e of 0.23.

4.2. Grid independence test and simulation validation

The complex geometry of Dixon rings made the implementation of structured meshes challenging. Therefore, unstructured grids of free tetrahedral elements were used for the fluid domains and triangular elements covered the surfaces. To ensure that the solution was independent of the size of the mesh used in the simulation, the grid independence (GR) test for different cell sizes was conducted. The properties of several meshes are presented in Table 3. The number of cells and the sizes of the elements that were used enabled the assessment of the resolution of the flow pattern.

When GR1 was tested, the liquid flow over Dixon rings did not change over time (Fig. 6 (a–e)). As expected, GR1 results did not produce any liquid penetration through the Dixon rings. The refined mesh (i.e. GR2) is described in Fig. 6 (f–j) illustrating a realistic pattern for the flowing liquid. Further increase in the number of elements (*i.e.* GR3) augmented the computational time with no clear discrepancies in the flow pattern observed, as shown in Fig. 6 (k–o) and therefore GR2 was adopted for the simulation study. The computation time ranged from 672 to 840 h at W_e = 0.23 to 2.57.

The refined mesh domain (i.e. GR2) is described in Fig. 7. This observation is confirmed by the trends of wetting efficiency with time illustrated in Table 4 where GR2 and GR3 demonstrated close performance. To ensure that the model replicates realistic flow, a segment of a larger sized Dixon ring was used for the simulation. The mesh used for this investigation, GR2-1, had the same properties as GR2 except for the larger number of cells, as shown in Table 3. Fig. 8 confirmed the trend observed in Fig. 5, which were driven by a hydrophilic pattern, similar to the one produced using GR2.

Table 3: Mesh properties for the CFD model discretisation.

Mesh type	Maximum element size (mm)	Minimum element size (mm)	Resolution of narrow regions (-)	Number of cells (cell)	Element size near Dixon rings wall (mm)
GR1	0.48	0.144	0.6	260798	0.06
GR2	0.322	0.096	0.7	586524	0.04
GR3	0.288	0.072	0.75	1008754	0.03
GR2-1	0.322	0.096	0.7	849542	0.05

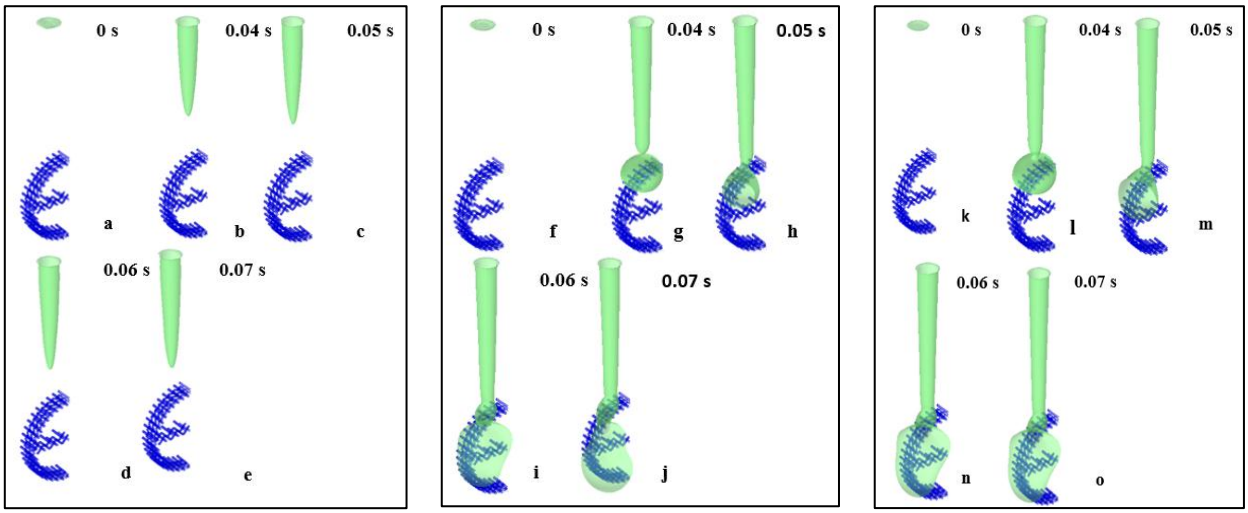

Fig. 6: Flow pattern of VOF = 0.5 for uncoated Dixon rings using grid GR1 (a-e), GR2 (f-J) and GR3 (k-o), (a,f,k) at 0 s, (b,g,l) at 0.04 s, (c,h,m) at 0.05 s, (d,i,n) at 0.06 and (e,j,o) at 0.07 s, W_e= 1.26 and θ = 105°

Table 4: Quantitative comparison using the wetting efficiency against time (s) for several mesh types.

Mesh type	**t (s)**	**0.03**	**0.04**	**0.05**	**0.06**	**0.07**
GR1	Wetting efficiency (-)	0	0.002	0.02	0.033	0.045
GR2		0	0.037	0.027	0.04	0.049
GR3		0	0.038	0.027	0.042	0.047

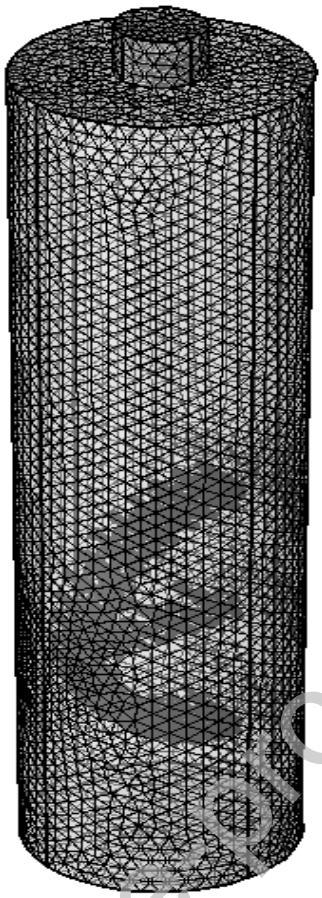

Fig. 7: Illustration of a domain of GR2 mesh.

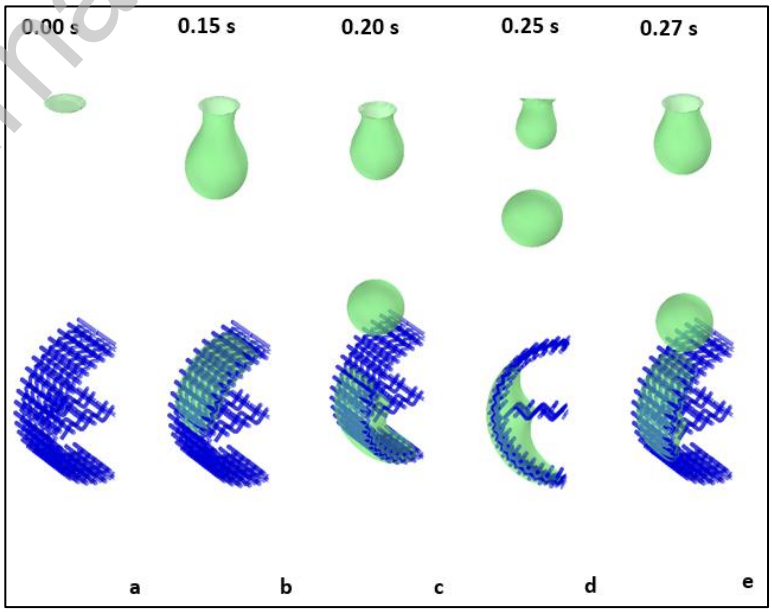

Fig. 8: Flow pattern of VOF = 0.5 for uncoated Dixon rings using the grid GR2-1, W_e= 0.23 and θ = 60°: (a) 0 s, (b) 0.04 s, (c) 0.05 s, (d) 0.06 and (e) 0.27 s.

4.3. Flow around coated Dixon rings

Fig. 9 (a,b) shows a scanning electron microscope image of a coated Dixon ring. The coating was concentrated in the areas near the pores and an area where wires intersect. Energy-dispersive X-ray spectroscopy (EDS) tests showed the molar percentage of 8% alumina of coating at the convex area of the wires, as described in the previous work [31]. These surface non-uniform distributions of the coating will have an impact on fluid flow through the opening as discussed in the following section.

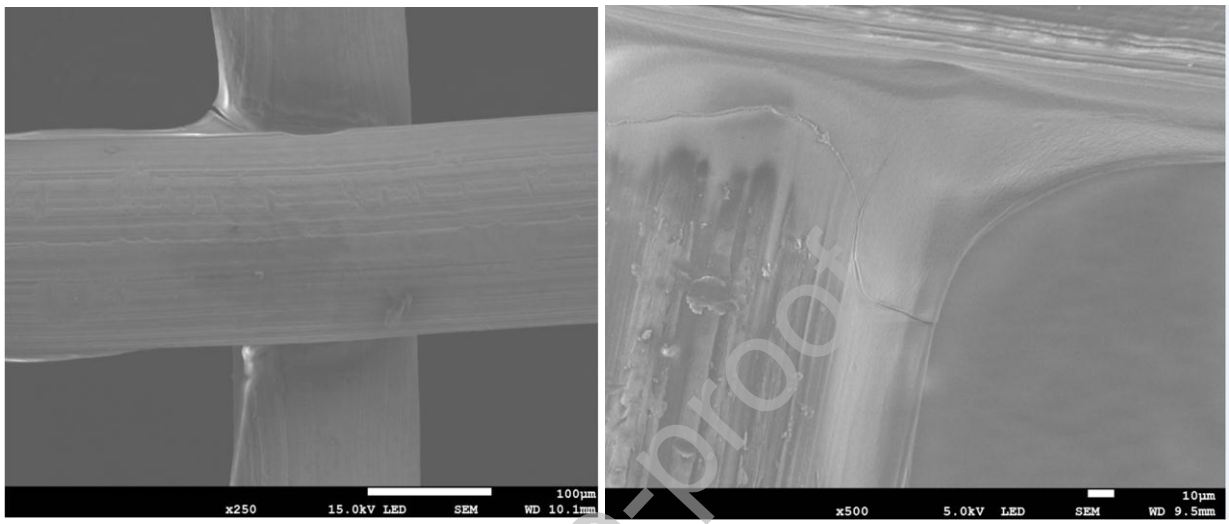

Fig. 9: Scanning electron microscopic image for coated Dixon ring: (a) ×250 and (b) ×500.

The flow around the coated Dixon rings was assessed by the experimental flow analysis and the VOF simulation. The static contact angle of the coated Dixon ring was challenging to assess experimentally due to the complex geometry of the stainless-steel grid.

To confirm the contact angle θ of the coated Dixon rings, the results of the laboratory observations of three depositions of alumina were compared to those obtained by simulation for different contact angles, ranging from hydrophilic to hydrophobic nature (i.e. 60 to 120°). Among these, the one based on a static contact angle $\theta = 105°$ demonstrated flow patterns similar to the experiments on coated Dixon rings.

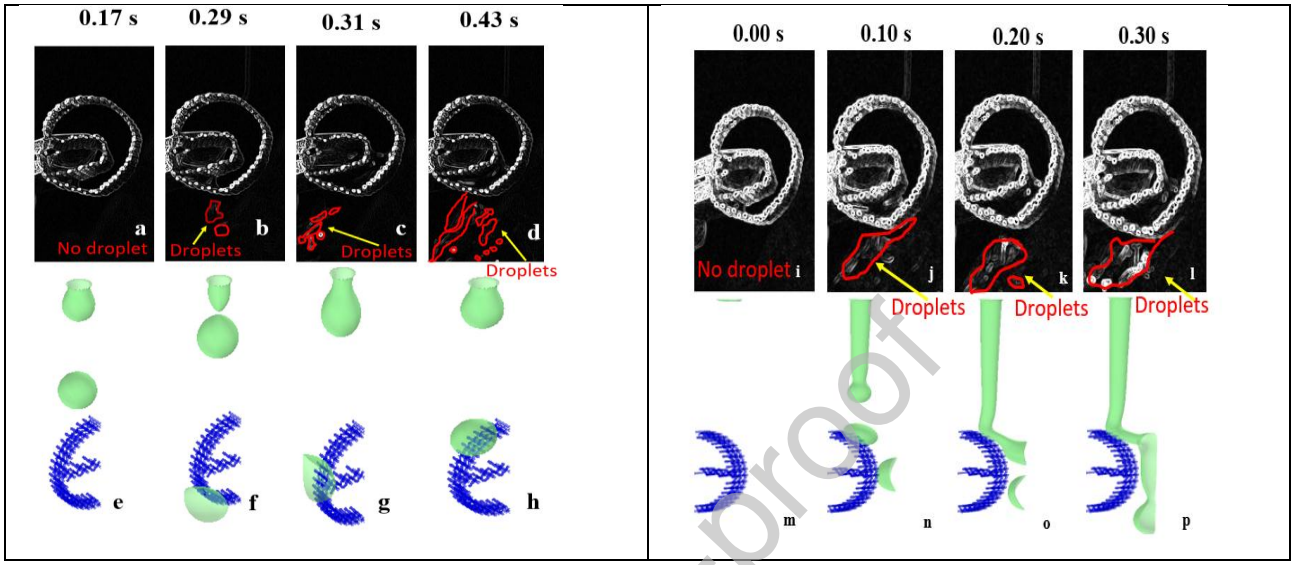

Fig. 10: Flow pattern by the experimental and simulation obervations: Snapshots of impact of droplets on coated stainless steel Dixon rings: θ = 105°, W_e= 0.23 (a-h) and W_e= 0.64 (i-p)

As shown in Fig. 10(a-h), at W_e= 0.23 and at 0.17 s, both experimental and simulation results show that capillary droplets were about to impinge the Dixon ring. The experimental droplet was repelled by the surface at 0.31 s while the simulation droplet was repealed at 0.29 s. The droplet accumulated at the top surface of the ring where the surface energy was high and the thickness of the liquid reached a maximum value, promoting then gravitational forces and leading the droplet to slip over the vertical curvature and detached at the bottom surface of the ring. Both the model and the experiments showed no penetration of the liquid into the grid of the coated Dixon ring, owing to its hydrophobic nature. Minor differences in the flow pattern occurred due to the non-uniformity of the contact angle, which made the droplet move around the Dixon ring until being forced to detach by the next droplet at 0.43 s and 0.29, as shown in Fig. 10 (d) and (f), respectively.

At $W_e$value of 0.64, the droplet accumulated at the top surface of the ring at a higher rate in comparison with the surface energy, accelerating the gravitational forces and detachment at the bottom surface of the ring. Few discrepancies were observed between the model results and the experiments, as illustrated in Fig. 10 (i-p). The analysis focused on understanding the relationship between the nature of the packing (i.e. hydrophobic or hydrophilic) and the changes in the flow

pattern over time. The images taken by the camera showed similar shapes to the droplets by simulation except for a minor amount of liquid that penetrated the Dixon rings opening, as shown in Fig. 10 (i). This disagreement could be caused by some assumptions used in the CFD simulation (i.e. the initial wall boundary conditions, constant wetted wall angle instead of a dynamic one with associated hysteresis and phase properties).

Fig. 10 (o & p) shows an average thickness over the length of the liquid film of 2 mm. Some tails are also observed which indicate the formation of a successive bubble that does not pass the mesh of the packing. Liquid-solid frictions led to extended droplets of lower local velocity compared with relevant bulk velocity. At a W_e value of 0.23, phenomena of shrinkage and spreading over the sides of the Dixon rings were not observed, demonstrating the relevance of inertial forces over the surface tension forces. Overall, the flow over the coated and the uncoated Dixon rings has shown that the coated version offered liquid spreading over the mesh opening in comparison with the uncoated one which offered more film flow that passed through the meshes for improved wettability.

4.4. Wetting efficiency by a parametric study

4.4.1. Influence of liquid inlet velocity

The wetting efficiency is defined as the ratio of the wetted area over the total area of packing. The effect of velocity u_o on the wetting efficiency was studied for the coated and uncoated rings. The profiles of wetting efficiency were calculated by averaging the liquid volume fraction (V_{f_1}) over the surface of the coated or uncoated rings with respect to time, as summarised in Fig. 11 and Fig. 12. Two distinctive peaks appeared for u_o = 0.15 m/s, each peak corresponded to dynamic profiles of wetting efficiency of the coated and uncoated rings with time and inlet liquid velocity and more relevant Figures of dynamics of the impact of the droplets with time were added (A 1). The liquid velocity was varied at 0.15, 0.25, 0.35 and 0.5 m/s. The velocity values of 0.15, 0.25 and 0.35 m/s corresponded to a dropwise flow from the nozzle while the velocity of 0.5 m/s corresponded to a jet flow from the nozzle. The residence time was approximately 0.05 s (i.e. first peak initiated at 0.15 s and ended at 0.2 s while the second peak started at 0.25 s and ended at 0.3 s). Conversely, five peaks appeared for the uncoated rings. The wetting efficiency reached a steady-state pattern after approximately 0.3 s. As shown in Fig. 12, the residence time for a single peak is 0.09 s, which is three times higher than that of the coated rings.

As shown in Fig. A1 (c), in appendix A, the droplet hit the Dixon ring at 0.14 s at high wetting efficiency but was then repelled by the hydrophobic nature of the ring at 0.15 s. As shown in Fig. A2 (g-l), when u_o was increased to 0.25 m/s, the drag forces destabilised the liquid stream by

delaying the outer layers of flow in respect to the inner ones, driving the cohesive molecular forces to become tenuous. The slower outer molecules dragged the inner molecules until the surface tension forces have exceeded the inertial forces [32]. At u_o of 0.35 m/s, the flow pattern changed because the surface tension forces were not dominant. The dynamic profiles of wetting efficiency of the coated rings with time and inlet liquid velocity are summarised in Fig. A3. The profiles of wetting efficiency are similar to those observed in the coated rings, but the residence time of the droplets of the uncoated Dixon rings was longer than that of the coated rings due to stronger adherence of the droplets to the rings, slowing down their travel inside the rings. At high liquid rates in both cases of coated and uncoated rings, the inertial forces dominated over the surface forces, resulting in the steady-state profile. It was not surprising to find that the wetting efficiency increased with u_o, which agreed with the work reported by Du *et al*. [10] confirming that u_o and the time required to reach the steady-state were directly proportional to each other. Overall, the high-velocity values stabilised the liquid shape of both uncoated and coated Dixon rings. The flow around the uncoated Dixon ring was converted into a film flow of uniform thickness due to a significant change in velocity over local parts of the droplets (i.e. increased thickness of the rolling droplet with reduced changes of the local parts).

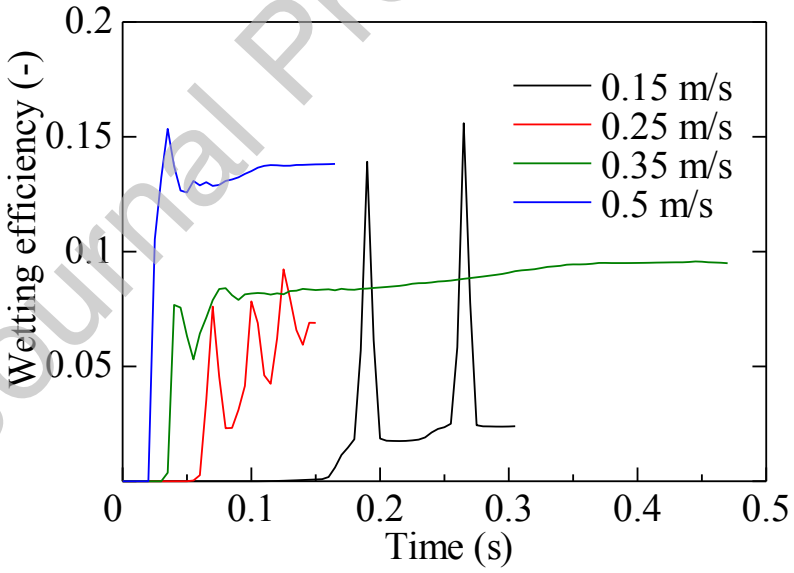

Fig. 11: The wetting efficiency profile for u_o = 0.15 m/s (black line), 0.25 m/s (red line), 0.35 m/s (green line) and 0.5 m/s (blue line) for coated rings, θ = 105°.

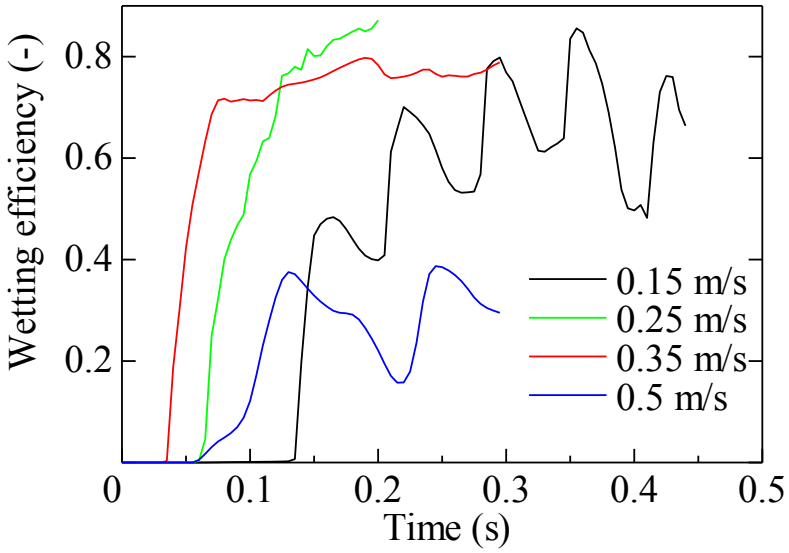

Fig. 12: The wetting efficiency profile for u_o = 0.15 m/s (black line), 0.25 m/s (green line), 0.35 m/s (red line) and 0.5 m/s (blue line) for uncoated rings, θ = 60°.

4.4.2. Influence of contact angle

The influence of contact angle on the wetting of Dixon rings was investigated for a reference velocity u_o of 0.15 m/s. The droplet dynamics for the actual coated ring (θ = 105°) and uncoated rings (θ =60°) were evaluated. Two additional values of the contact angle at 90° and 120° were also simulated, allowing observation of the behaviour of flow through the opening and flow over the surface of Dixon rings, prediction of the flow over more hydrophobic and hydrophilic conditions, that is a higher angle than 120° and lower than 60°, respectively, reproducing phenomena of solvent-surface interactions of a wide range of industrial applications [33].

At the value of θ = 60°, which corresponds to the uncoated Dixon ring, the droplet adhered to the ring, spread over to achieve maximum wetting and passed through the mesh opening, as illustrated in Fig. 13 (a). At θ = 90°, the droplet passed through the mesh opening of the Dixon rings but with less wetting, as shown in Fig. 13 (b) and then was repelled at long residence times in the Dixon ring. These trends continued at higher contact angles (i.e. θ = 105° and 120°) where the droplet observed no bouncing on the Dixon ring wall but a weaker adherence to the rings and more rolling over the wall of the rings, resulting in the lowest wetting efficiency, as shown in the wetting profile in Fig. 14.

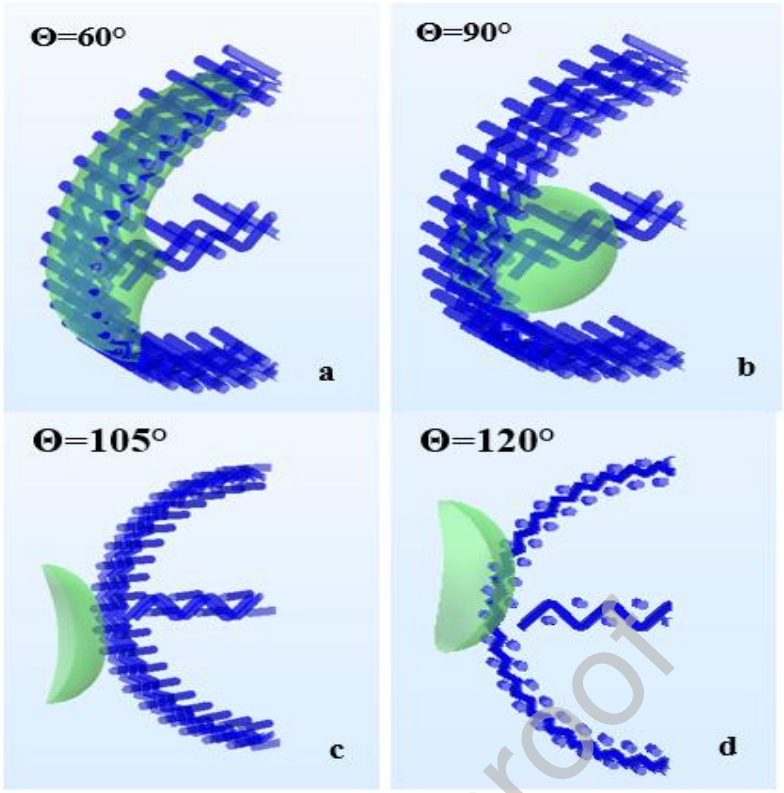

Fig. 13: Flow pattern of VOF = 0.5 at 0.14 s using the grid GR2, *We* = 0.23 for θ: (a) 60° (uncoated Dixon rings); (b) 90°; (c) 105° (coated Dixon rings); (d) 120°.

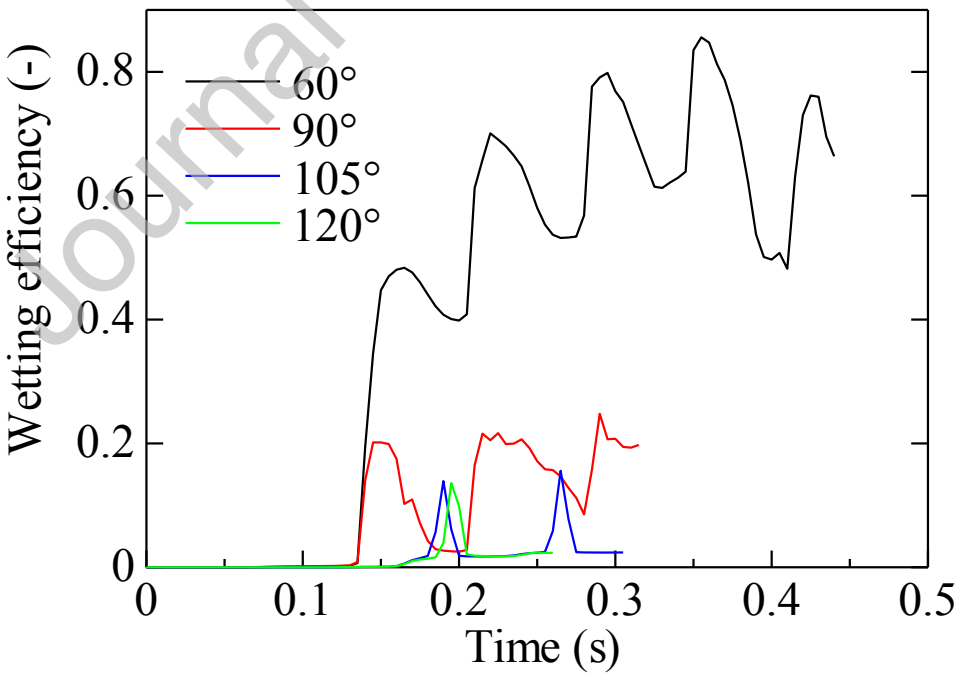

Fig. 14: The wetting efficiency of Dixon rings, *We* = 0.23 for θ = 60° (black line), 90° (red line), 105° (blue line) and 120° (green line).

4.5. Hydrodynamic performance

4.5.1. Liquid holdup

The liquid holdup was obtained by averaging the volume of the liquid volume fraction (V_{f_1}). The liquid holdup (h_l) was studied for Weber number (W_e) 0.23 to 2.57 for θ = 60°, 90°, 105° and 120°, as shown in Fig. 15 and Fig. 16. The trend for h_l was similar to the wetting efficiency profiles, when the wetting efficiency increased, the liquid holdup increased and therefore $h_l$increased with W_e and reduced contact angles. The liquid holdup for the uncoated Dixon rings (i.e θ = 60°) is the highest among all, as shown in Fig. 15. A minor discrepancy was found at W_e = 2.66, θ = 90° had the highest liquid holdup. This is a consequence of numerical modelling and could be explained by the fact that more liquid was allowed, which is particularly true in the range of contact angle from 90° to penetrate the mesh opening, while some adherence of the liquid is observed for the uncoated Dixon rings at θ = 105°.

The results from the VOF model were compared to models usually used in literature for random packing structure (i.e. Stichlmair *et al*. [34] by Equations (13) and (14) and Billet & Schultes [4] by Equation (15)), as illustrated in Fig. 16 (a-d). The model results for h_L were fitted to Stichlmair *et al*. [34] using 2-D curve-fitting on Matlab. An exclusive correlation for the liquid holdup for Dixon ring, is shown in Equation (13). The model constant had 95% confidence bounds, b = 0.226, c = 0.08083 and R-square= 0.9557. The results for θ = 60°, 90°, 105° and 120° are in a reasonable agreement with those by Stichlmair's model, particularly in the hydrophilic zone of the contact angle 60° and 90°, as shown in Fig. 16 (a) and (b), respectively. The comparison for hydrophilic Dixon rings showed that Stichlmair *et al*. [34] model is reliable at low W_e (i.e. the relative deviation of 7.21 % at θ = 60° and 14.12 % for θ = 90°). The reliability of the CFD model decreased at high W_e (i.e. relative difference was low for all W_e except at W_e= 2.66 where it reached deviation of 42.31 %). At θ = 105° and 120°, as shown in (c) and (d), both Stichlmair *et al*. [34] and Billet models showed poor predictions, the relative difference errors being 24.01% and 33.23%, confirming additional local mixing could take place.

$$h_L = 0.080\ {F_{r_L}}^{0.22} \quad (13)$$

$$F_{r_L} = \frac{{u_0}^2 a_p}{g} \quad (14)$$

$$h_L = 12\left(\frac{\vartheta}{g\rho_L} u_0 {a_p}^2\right)^{1/3}\left(\frac{a_e}{a_p}\right) \quad (15)$$

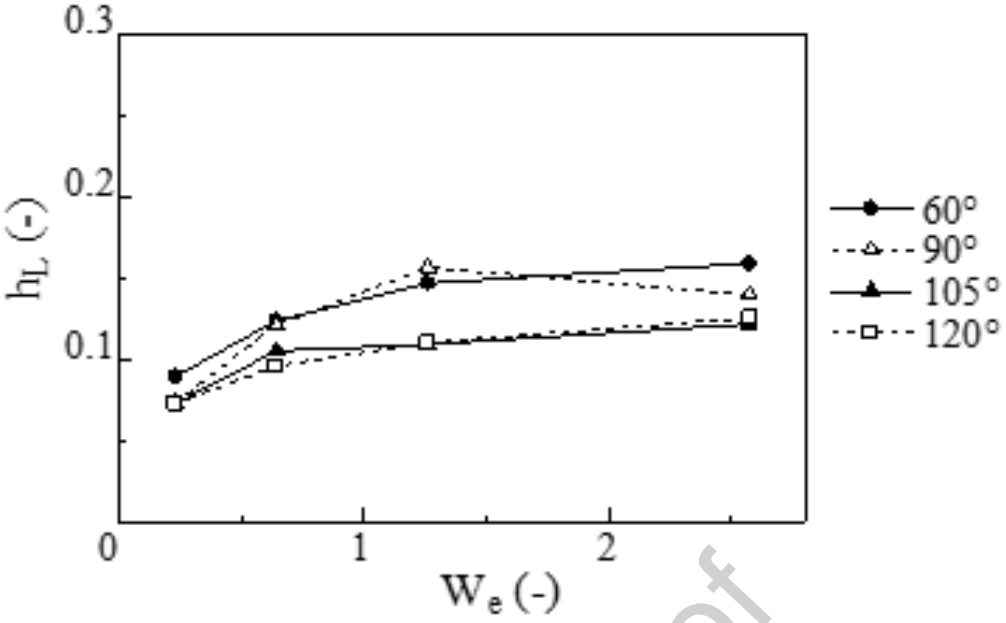

Fig. 15: Effect of Weber number (W_e) on the liquid holdup (h_l) for uncoated Dixon rings, θ = 60° (filled circles), 90° (hollow triangles), 105° (filled triangles) and 120° (hollow squares).

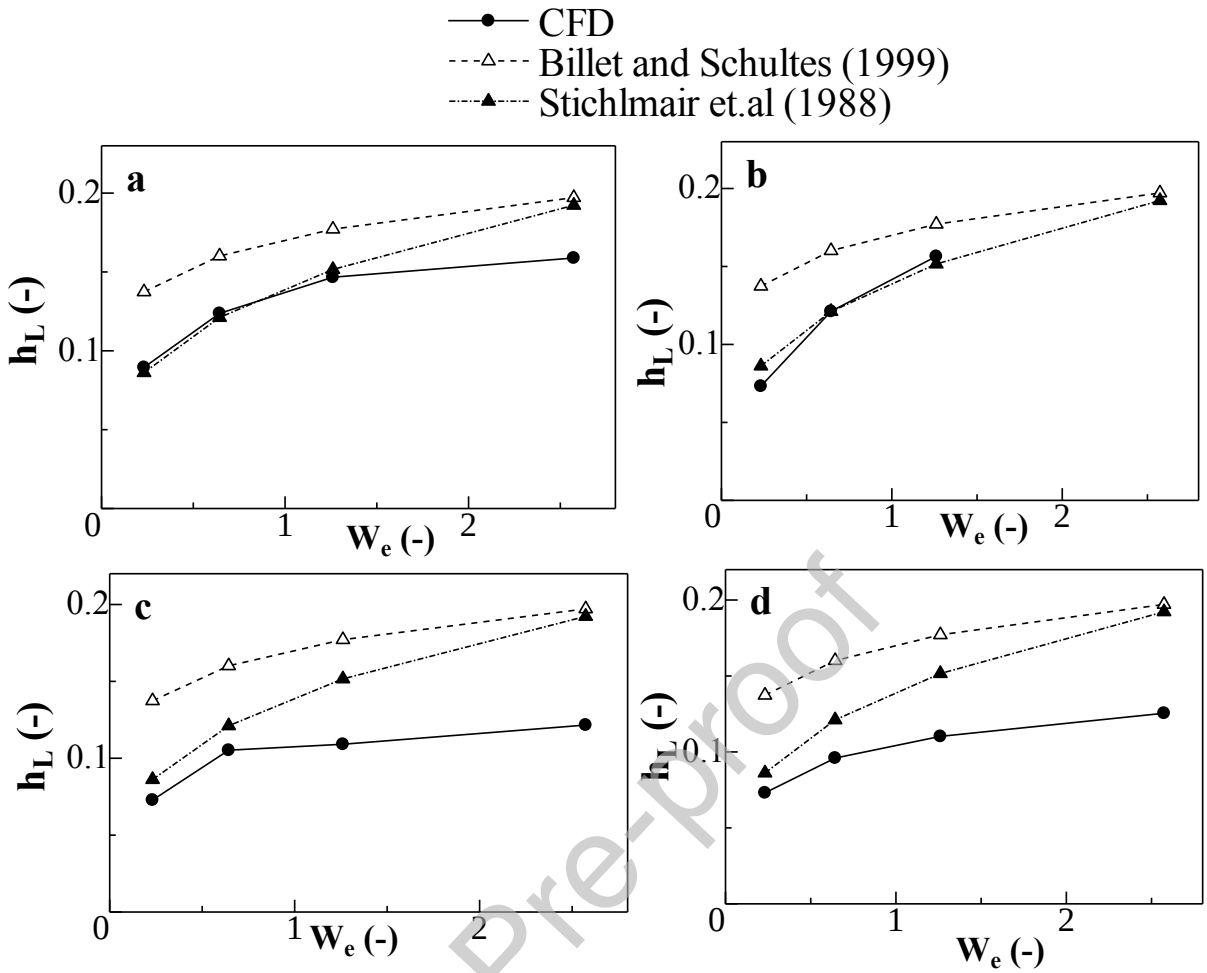

Fig. 16: Effect of Weber number (W_e) on the liquid holdup (h_l): a) θ = 60°; b) θ = 90°; c) θ = 105°; d) θ = 120°. CFD model (filled circles), Billet & Schultes [4] (hollow triangles) and Stichlmair *et al*. [34] (filled triangles).

4.5.2. Effective surface area

The effective area, which is a critical parameter in gas-liquid mass transfer operations, was calculated by averaging the liquid volume fraction (V_{f_1}) and dividing by the surface of the Dixon ring. The effective area (a_e) was studied for a range of Weber number between $W_e = 0.23$ and 2.57 and contact angle of θ = 60°, 90°, 105° and 120°, as illustrated in Fig. 17. The general trend shows the effective area increased with W_e. The highest effective area is at θ = 60°, while the lowest is at $\theta = 120°$, except for $W_e = 0.23$, the effective area at 105° is lower than that of 120° with a value of 0.031.

These results were compared to Linek *et al*. [35] given by Equation (16) and Billet & Schultes [4] given by Equation (17), for θ = 60°, θ = 90°, θ = 105° and θ = 120°, as shown in Fig. 18 (a-d). Billet & Schultes [4] requires additional physical parameters such as density (ρ_L) and viscosity (u_L). The

results obtained using the CFD modelling were closer to the model by Linek (i.e. relative difference error for Linek *et al*. [35] model are 15.40% at θ = 60° and 14.24% for θ = 90°). Billet & Schultes [4] were higher than 40% for most of the contact angles but at θ = 105° and 120°, the relative deviations were 31.05 % and 15.32%. This shows that Linek *et al*. [35] was more reliable to predict the effective area for Dixon rings.

$$\frac{a_e}{a_p} = 0.0277\left(\frac{1+cos\theta}{2}\right)^{3.477}\left(a_p d_p\right)^{1.585}\left(\frac{\rho_L u_0}{a_p \mu_L}\right)^{0.641-0.407\left(\frac{1+cos\theta}{2}\right)} \quad (16)$$

$$\frac{a_e}{a_p} = 1.5\left(a_p d_p\right)^{-0.5}\left(\frac{u_0 d_p}{\mu_L}\right)^{-0.2}\left(\frac{\rho_L d_p {u_L}^2}{\sigma_L}\right)^{0.75}\left(\frac{{u_L}^2}{g d_p}\right)^{-0.45} \quad (17)$$

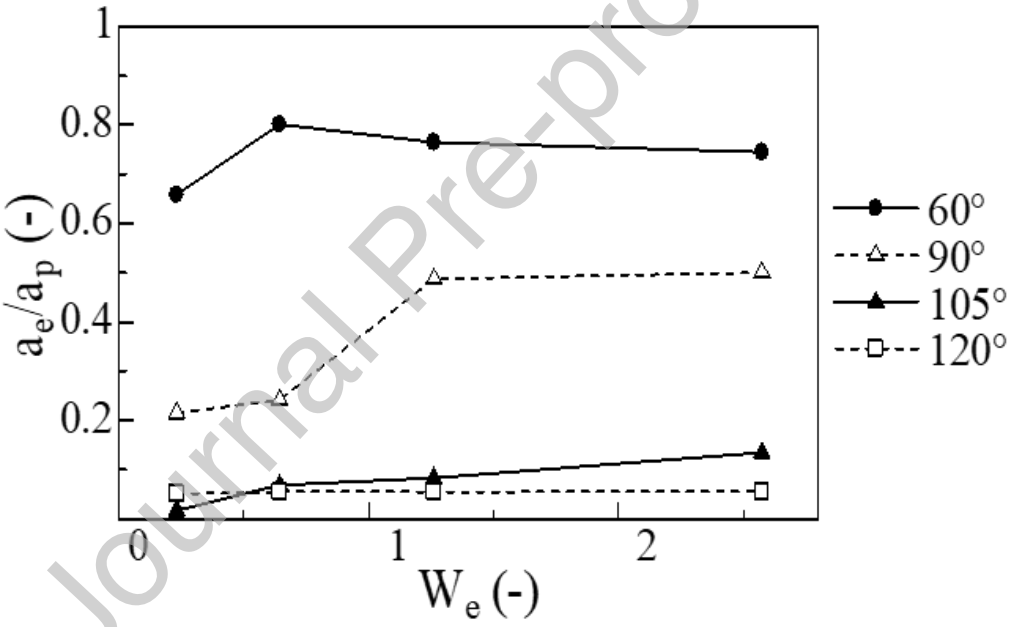

Fig. 17: Effect of Weber number (W_e) on the normalized effective area for uncoated Dixon rings, θ = 60° (filled circles), 90° (hollow triangles), 105° (filled triangles) and 120° (hollow squares).

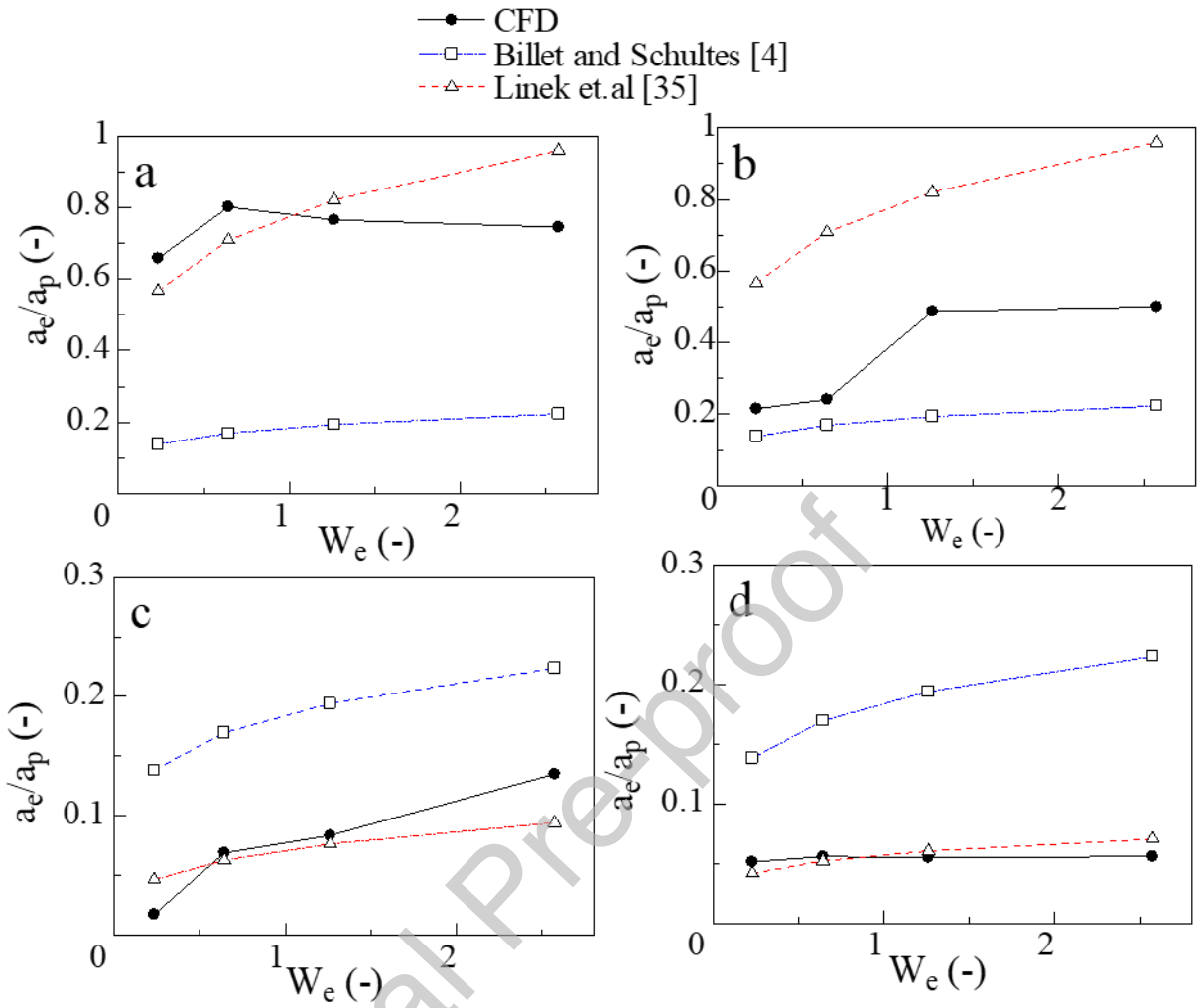

Fig. 18: Effect of Weber number (W_e) on the normalised effective area for: a) θ = 60° b) θ = 90° c) θ = 105° d) θ = 120°, CFD model (filled circles), Linek *et al*. [35] (hollow triangles) and Billet & Schultes [4] (hollow squares).

5. Conclusions

This work demonstrated the role of flow at pore-scale of low flow regime operations inside the packed beds on control of wettability, holdup and the effective area for Dixon packing. It offers options to design packing for gas-liquid separation applications with tuneable opportunities for packing wettability and liquid mixing. The liquid flow over a single Dixon ring was studied using laboratory imaging experiments and 3D simulations. The investigation was conducted on a single wire mesh uncoated and surface modified Dixon ring with an alumina coating. The results of the VOF model were validated by imaging of the flow using a CCD camera and by a grid test simulation solution that was independent of the number of cells.

A cycle of droplet flow over an uncoated Dixon ring exhibited penetration of the hydrophilic mesh openings, adherence to the surface of the ring, obstruction by the horizontal grid at the centre of the ring and accumulation at the bottom region of the Dixon rings. The adherence of the droplet to the Dixon ring confirmed the hydrophilic nature of the Dixon ring. The cycle of the droplet interaction with the uncoated hydrophobic Dixon ring exhibited accumulation of the droplet at the top surface of the ring where the thickness of liquid reached a maximum value. This has promoted the gravitational forces and led the droplet to slip over the vertical curvature to the bottom surface of the ring without any penetration inside the ring.

The droplets profiles for the coated and uncoated rings were obtained by experiments and CFD simulations, and these were in reasonable agreement which allowed the further parametric study of the impact of the flow and contact angle on the wetting efficiency, liquid holdup and effective surface area. The uncoated Dixon rings were found to have a contact angle of 60° which described a hydrophilic packing nature, promoting the wetting efficiency by making the droplet to spread over it. The coated rings were shown to be hydrophobic in nature (contact angle of 105°), promoting repellence of the droplets. The time needed to reach the steady-state decreased when the liquid inlet velocity was increased or the contact angle was decreased. High flow rates destabilised the liquid stream by delaying the outer layers of flow with respect to the inner ones, driving the cohesive molecular forces to become tenuous.

The 3D CFD model confirmed the increase in the wetting efficiency, liquid holdup and effective surface area with increased liquid flowrate and reduced contact angle, in reasonable agreement with Stichlmair's model, particularly in the hydrophilic zone of the contact angle and low W_e and Linek's model, particularly in the hydrophobic range of the contact angle. This was driven by the development of a film of uniform thickness over the coated ring and by an increase in the thickness and length of the droplet over the uncoated rings. The high wettability and the hydrophilic nature of the uncoated Dixon rings can reduce the operational condition in packed columns. The hydrophobic coatings can be implemented in gas-liquid separation processes that require high mixing in packed beds.

Declaration of Competing Interest

The authors declare that they have no known competing financial interests or personal relationships that could have appeared to influence the work reported in this paper.

Acknowledgements

The authors acknowledge the financial support from the Centre for Global Eco-Innovation at Lancaster University, the European Regional Development Fund (Grant Reference: 03R17P01835 – Eco-Innovation Cheshire and Warrington) and Croft Filters Ltd, Risley, UK.

Appendix A

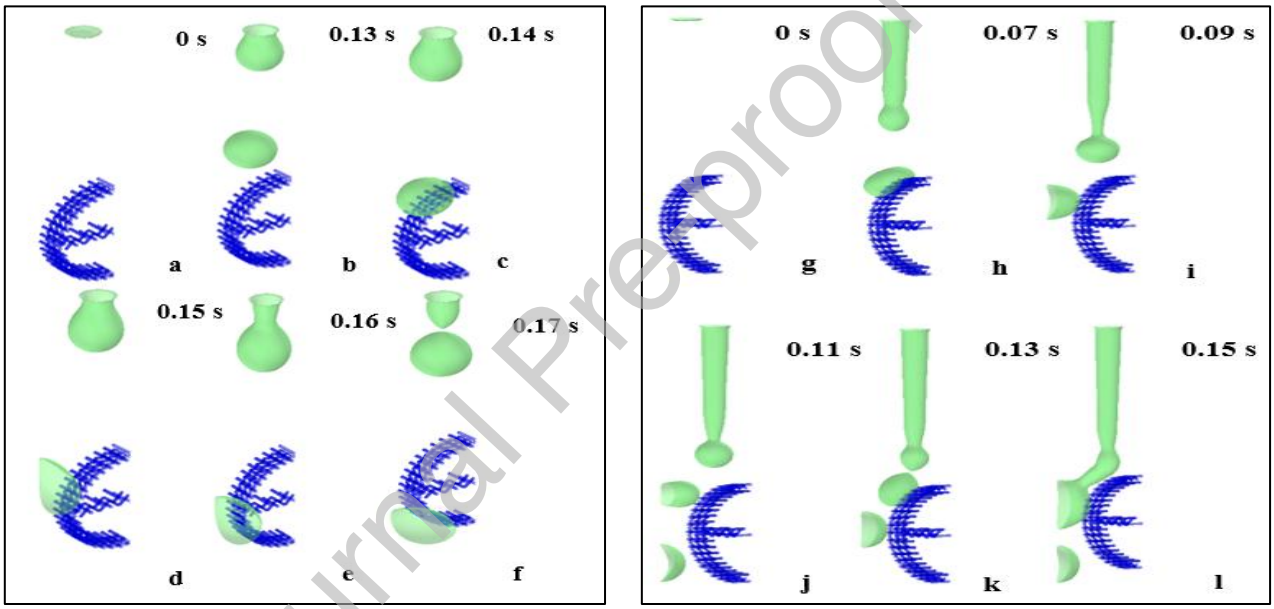

Figure A1 : Flow pattern of VOF = 0.5 for Dixon rings using the grid GR2, for coated rings, θ = 105° for u_o = 0.15 m/s: (a) 0 s, (b) 0.13 s, (c) 0.14 s, (d) 0.15 s, (e) 0.16 s and (f) 0.17 s, and , and u_o = 0.25 m/s: (g) 0 s, (h) 0.07 s, (i) 0.09 s, (j) 0.11 s, (k) 0.13 s and (l) 0.15 s.

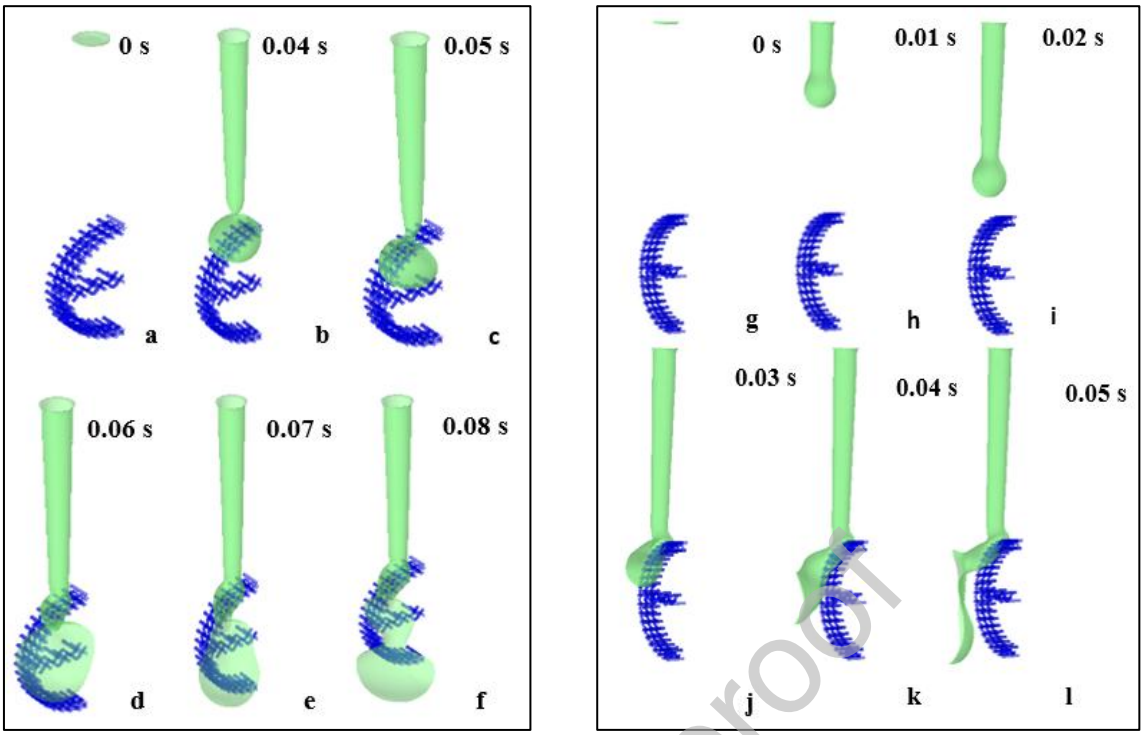

Figure A2 : Flow pattern of VOF = 0.5 for Dixon rings using the grid GR2, u_o = 0.35 m/s for coated rings, θ = 105°: (a) 0 s, (b) 0.04 s, (c) 0.05 s, (d) 0.06 and (e) 0.07 s and (f) 0.08 s. °: uo = 0.5 m/s (g) 0 s, (h) 0.01 s, (i) 0.02 s, (j) 0.03 and (k) 0.04 s and (l) 0.05

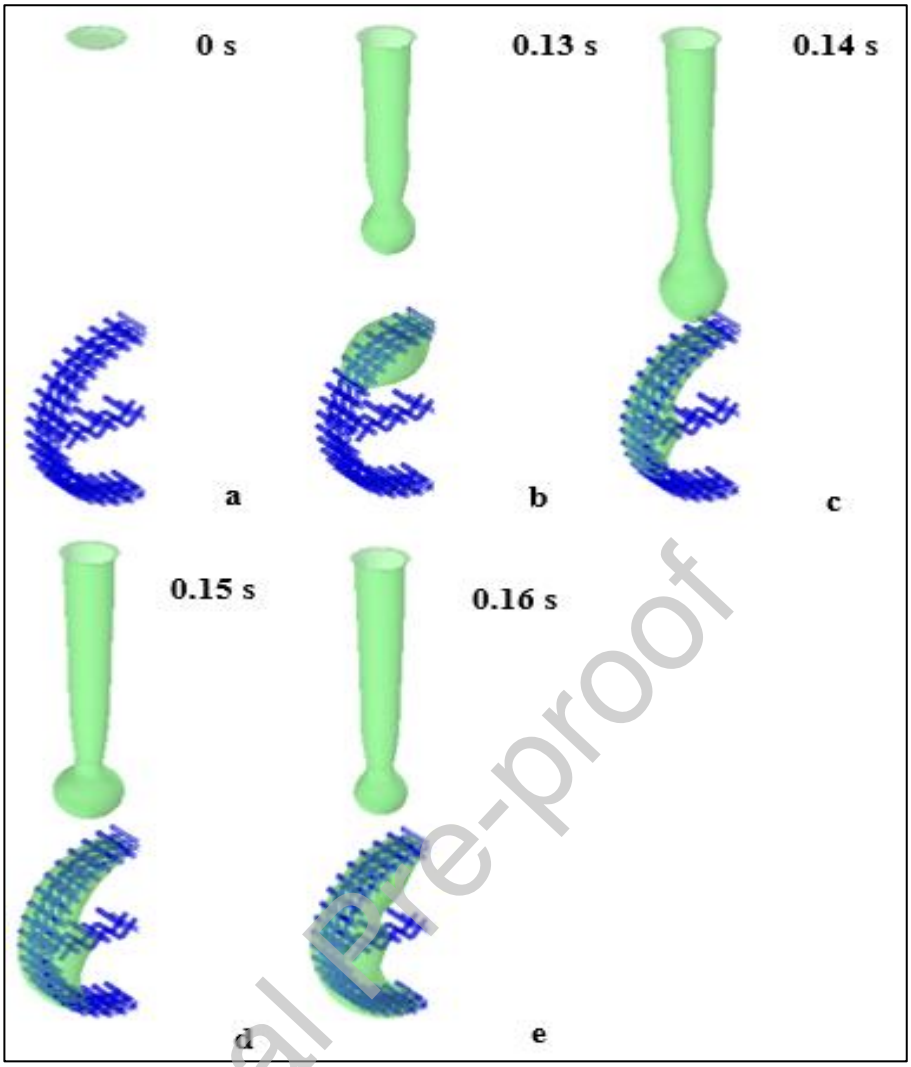

Figure A3: Flow pattern of VOF = 0.5 for Dixon rings using the grid GR2, u_0 = 0.25 m/s for uncoated rings, θ = 60°: (a) 0 s, (b) 0.13 s, (c) 0.14 s, (d) 0.15 s, (e) 0.16 s.

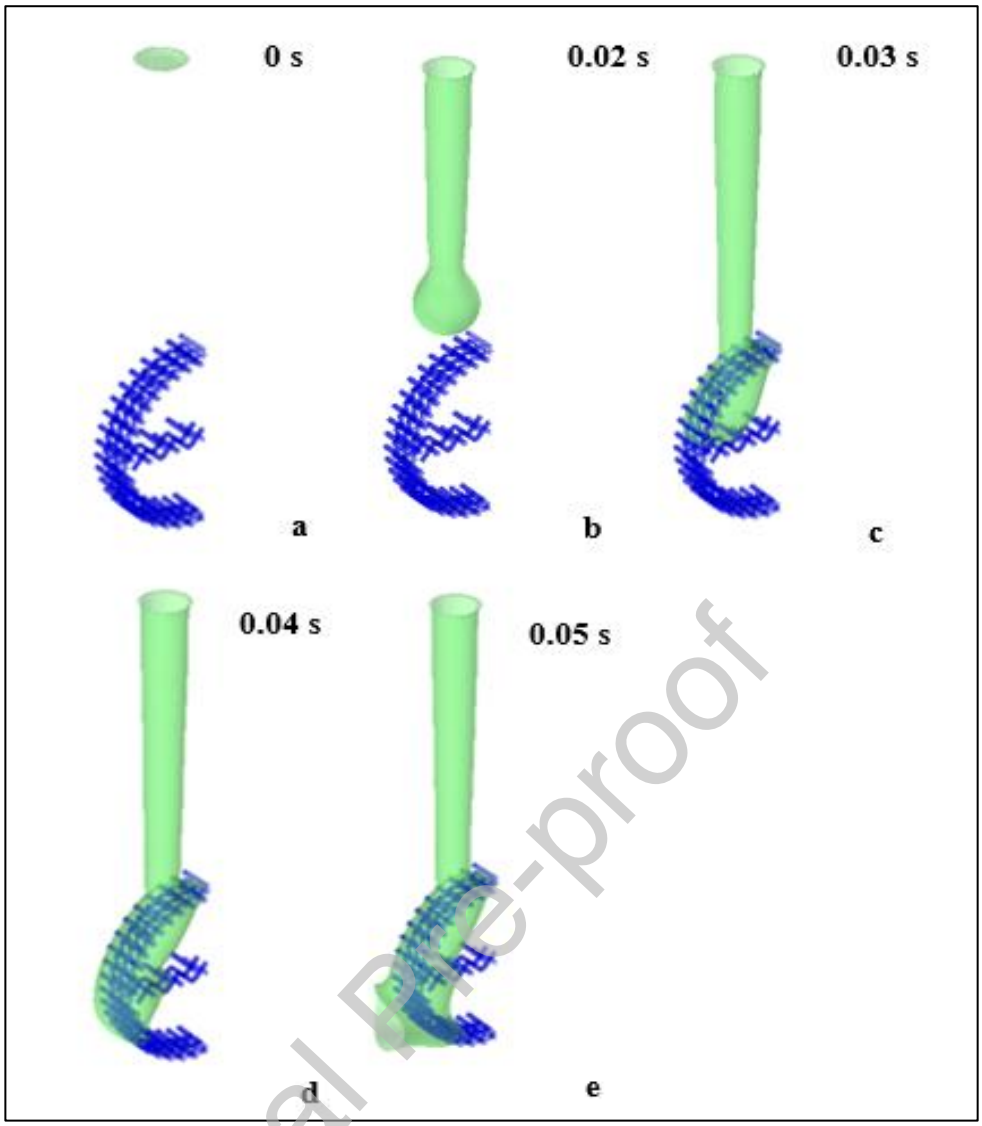

Figure A4: Flow pattern of VOF = 0.5 for Dixon rings using the grid GR2, u_o = 0.5 m/s for uncoated rings, θ = 60°: (a) 0 s, (b) 0.01 s, (c) 0.02 s, (d) 0.03 and (e) 0.04

References

[1] J.J. Llano, R. Rosal, H. Sastre, F. V. Díez, Determination of Wetting Efficiency in Trickle-Bed Reactors by a Reaction Method, Ind. Eng. Chem. Res. 36 (1997) 2616–2625. https://doi.org/10.1021/ie960435o.

[2] V. Sodhi, Trickle/pulse flow regime transition in downflow packed tower involving foaming liquids, Chem. Ind. Chem. Eng. Q. 18 (2012) 349–359. https://doi.org/10.2298/ciceq111201011s.

[3] P. Yan, X. Li, H. Li, Y. Shao, H. Zhang, X. Gao, Hydrodynamics and mechanism of

hydrophobic foam column tray: Contact angle hysteresis effect, AIChE J. 66 (2020) 1–11. https://doi.org/10.1002/aic.16793.

[4] R. Billet, M. Schultes, Modelling of pressure drop in packed columns, Chem. Eng. Technol. 14 (1991) 89–95. https://doi.org/10.1002/ceat.270140203.

[5] J.A. Rocha, J.L. Bravo, J.R. Fair, Distillation columns containing structured packings: A comprehensive model for their performance. 2. Mass-transfer model, Ind. Eng. Chem. Res. 35 (1996) 1660–1667. https://doi.org/10.1021/ie940406i.

[6] C.K. Lambert, R.D. Gonzalez, Effect of Gd2O3 and Sm2O3 addition on the properties of CeO2, J. Korean Inst. Electr. Electron. Mater. Eng. 16 (2003) 979–986. https://doi.org/10.4313/JKEM.2003.16.11.979.

[7] Z. Dong, L. Wu, J. Wang, J. Ma, L. Jiang, Superwettability Controlled Overfl ow, Adv. Mater. (2015) 1745–1750. https://doi.org/10.1002/adma.201405387.

[8] Y. Haroun, L. Raynal, P. Alix, Prediction of effective area and liquid hold-up in structured packings by CFD, Chem. Eng. Res. Des. 92 (2014) 2247–2254. https://doi.org/10.1016/j.cherd.2013.12.029.

[9] A. Ataki, H.J. Bart, Experimental and CFD simulation study for the wetting of a structured packing element with liquids, Chem. Eng. Technol. 29 (2006) 336–347. https://doi.org/10.1002/ceat.200500302.

[10] W. Du, D. Feng, J. Xu, W. Wei, Computational Fluid Dynamics Modeling of Gas-Liquid Two-Phase Flow around a Spherical Particle, Chem. Eng. Technol. 36 (2013) 840–850. https://doi.org/10.1002/ceat.201200486.

[11] F. Augier, A. Koudil, A. Royon-Lebeaud, L. Muszynski, Q. Yanouri, Numerical approach to predict wetting and catalyst efficiencies inside trickle bed reactors, Chem. Eng. Sci. 65 (2010) 255–260. https://doi.org/10.1016/j.ces.2009.06.027.

[12] R. Kumar, H.J.P.V.K. Sharma, Investigation of hydrodynamic behaviour of a pilot-scale trickle bed reactor packed with hydrophobic and hydrophilic packings using radiotracer technique, (2012) 71–75. https://doi.org/10.1007/s10967-011-1512-1.

[13] P. Yan, X. Gao, Hydrodynamics and mechanism of hydrophobic foam column tray : Contact angle hysteresis effect, (2020) 1–11. https://doi.org/10.1002/aic.16793.

[14] J.P. Zhang, Y. Luo, G.W. Chu, L. Sang, Y. Liu, L.L. Zhang, J.F. Chen, A hydrophobic wire mesh for better liquid dispersion in air, Chem. Eng. Sci. 170 (2017) 204–212. https://doi.org/10.1016/j.ces.2017.03.058.

[15] C. Ma, M.J. Su, Y. Luo, G.W. Chu, B.C. Sun, J.F. Chen, Wetting behavior of the stainless steel wire mesh with Al2O3 coatings and mass transfer intensification in a rotating packed bed, Ind. Eng. Chem. Res. 59 (2020) 1374–1382. https://doi.org/10.1021/acs.iecr.9b04745.

[16] M. Su, S. Bai, Y. Luo, G. Chu, B. Sun, Y. Le, Controllable wettability on stainless steel substrates with highly stable coatings, 195 (2019) 791–800. https://doi.org/10.1016/j.ces.2018.10.025.

[17] Y. Wang, J. Chen, F. Larachi, Modelling and simulation of trickle-bed reactors using computational fluid dynamics: A state-of-the-art review, Can. J. Chem. Eng. 91 (2013) 136–180. https://doi.org/10.1002/cjce.20702.

[18] W. Du, L. Zhang, S. Lv, P. Lu, J. Xu, W. Wei, Numerical study of liquid coverage in a gas-liquid-solid packed bed, Particuology. 23 (2015) 90–99. https://doi.org/10.1016/j.partic.2014.10.013.

[19] G.M. Karthik, V. V. Buwa, Effect of particle shape on catalyst deactivation using particle-resolved CFD simulations, Chem. Eng. J. 377 (2019). https://doi.org/10.1016/j.cej.2018.10.101.

[20] R.K. Singh, J.E. Galvin, X. Sun, Multiphase flow studies for microscale hydrodynamics in the structured packed column, Chem. Eng. J. 353 (2018) 949–963. https://doi.org/10.1016/j.cej.2018.07.067.

[21] Y. Liu, Y. Luo, G.W. Chu, F. Larachi, H.K. Zou, J.F. Chen, Liquid microflow inside the packing of a rotating packed bed reactor: Computational, observational and experimental studies, Chem. Eng. J. 386 (2020) 121134. https://doi.org/10.1016/j.cej.2019.03.010.

[22] P. Yue, J.J. Feng, C. Liu, J. Shen, A diffuse-interface method for simulating two-phase flows of complex fluids, J. Fluid Mech. 515 (2004) 293–317. https://doi.org/10.1017/S0022112004000370.

[23] R. Maiti, A. Atta, K.D.P. Nigam, Effect of particle porosity on hysteresis in trickle-bed reactors, Ind. Eng. Chem. Res. 47 (2008) 8126–8135. https://doi.org/10.1021/ie8003539.

[24] R.M. Propp, P. Colella, W.Y. Crutchfield, M.S. Day, A Numerical Model for Trickle Bed Reactors, J. Comput. Phys. 165 (2000) 311–333. https://doi.org/10.1006/jcph.2000.6604.

[25] D. Jacqmin, Calculation of Two-Phase Navier – Stokes Flows Using Phase-Field Modeling, J. Comput. Phys. 127 (1999) 96–127.

[26] D. Janssen, R. De Palma, S. Verlaak, P. Heremans, W. Dehaen, Static solvent contact angle measurements, surface free energy and wettability determination of various self-assembled monolayers on silicon dioxide, Thin Solid Films. 515 (2006) 1433–1438. https://doi.org/10.1016/j.tsf.2006.04.006.

[27] M. Vonka, J. Kosek, Modelling the morphology evolution of polymer materials undergoing phase separation, Chem. Eng. J. 207–208 (2012) 895–905. https://doi.org/10.1016/j.cej.2012.06.091.

[28] L.J.S. Halloran, P. Brunner, D. Hunkeler, COMPEST, a PEST-COMSOL interface for

inverse multiphysics modelling: Development and application to isotopic fractionation of groundwater contaminants, Comput. Geosci. 126 (2019) 107–119. https://doi.org/10.1016/j.cageo.2019.02.001.

[29] A. Fortin, A. Zine, An improved GMRES method for solving viscoelastic fluid flow problems, J. Nonnewton. Fluid Mech. 42 (1992) 1–18. https://doi.org/https://doi.org/10.1016/0377-0257(92)80001-E.

[30] S.C. Beutelspacher, N. Serbecic, P. Tan, M.O. McClure, Vergleich verschiedener viraler vektoren zur gentherapie von hornhautendothelzellen, Ophthalmologe. 102 (2005) 1168–1174. https://doi.org/10.1007/s00347-005-1230-6.

[31] M. Abdelraouf, J. Hegarty, A. Rennie, R. Elizalde, N. Burns, L. Geekie, V. Najdanovic-Visak, F. Aiouache, Sol-gel alumina coating of wire mesh packing, Ceram. Int. (2020) 0–1. https://doi.org/10.1016/j.ceramint.2020.05.043.

[32] R.S. Volkov, G. V. Kuznetsov, P.A. Strizhak, Water droplet deformation in gas stream: Impact of temperature difference between liquid and gas, Int. J. Heat Mass Transf. 85 (2015) 1–11. https://doi.org/10.1016/j.ijheatmasstransfer.2015.01.078.

[33] M. Osękowska, E. Karuga-Kuźniewska, D. Wojcieszak, M. Mazur, A. Poniedziałek, D. Kaczmarek, M. Szymonowicz, Z. Rybak, Influence of nanocrystalline structure and surface properties of TiO2 thin films on the viability of L929 cells, Polish J. Chem. Technol. 17 (2015) 33–39. https://doi.org/10.1515/pjct-2015-0047.

[34] J. Stichlmair, J.L. Bravo, J.R. Fair, General model for prediction of pressure drop and capacity of countercurrent gas/liquid packed columns, Gas Sep. Purif. 3 (1989) 19–28. https://doi.org/http://dx.doi.org/10.1016/0950-4214(89)80016-7.

[35] V. Linek, P. Petricek, P. Benes, R. Braun, Effective interfacial area and liquid side mass transfer coefficients in absorption columns packed with hydriphilised and untreated plastic packings., Chem. Eng. Res. Des. 62 (1984) 13–21.